Article

Universal quantum logic in hot silicon qubits

https://doi.org/10.1038/s41586-020-2170-7

Received: 22 October 2019

Accepted: 22 January 2020

Published online: 15 April 2020

Check for updates

L. Petit[1], H. G. J. Eenink[1], M. Russ[1], W. I. L. Lawrie[1], N. W. Hendrickx[1], S. G. J. Philips[1], J. S. Clarke[2], L. M. K. Vandersypen[1] & M. Veldhorst[1]✉

Quantum computation requires many qubits that can be coherently controlled and coupled to each other[1]. Qubits that are defined using lithographic techniques have been suggested to enable the development of scalable quantum systems because they can be implemented using semiconductor fabrication technology[2–5]. However, leading solid-state approaches function only at temperatures below 100 millikelvin, where cooling power is extremely limited, and this severely affects the prospects of practical quantum computation. Recent studies of electron spins in silicon have made progress towards a platform that can be operated at higher temperatures by demonstrating long spin lifetimes[6], gate-based spin readout[7] and coherent single-spin control[8]. However, a high-temperature two-qubit logic gate has not yet been demonstrated. Here we show that silicon quantum dots can have sufficient thermal robustness to enable the execution of a universal gate set at temperatures greater than one kelvin. We obtain single-qubit control via electron spin resonance and readout using Pauli spin blockade. In addition, we show individual coherent control of two qubits and measure single-qubit fidelities of up to 99.3 per cent. We demonstrate the tunability of the exchange interaction between the two spins from 0.5 to 18 megahertz and use it to execute coherent two-qubit controlled rotations. The demonstration of 'hot' and universal quantum logic in a semiconductor platform paves the way for quantum integrated circuits that host both the quantum hardware and its control circuitry on the same chip, providing a scalable approach towards practical quantum information processing.

Spin qubits based on quantum dots are among the most promising candidates for large-scale quantum computation[2,9,10]. Quantum coherence can be maintained in these systems for extremely long times[11] by using isotopically enriched silicon (^{28}Si) as the host material[12]. This has enabled the demonstration of single-qubit control with fidelities exceeding 99.9%[13,14] and the execution of two-qubit logic[15–18]. The potential to build larger systems with quantum dots manifests in the ability to deterministically engineer and optimize qubit locations and interactions using a technology that greatly resembles present-day complementary metal-oxide semiconductor (CMOS) manufacturing. Nonetheless, quantum error correction schemes predict that millions to billions of qubits will be needed for practical quantum information processing[19]. Considering that existing devices use more than one terminal per qubit[20], wiring up such large systems remains a formidable task. To avoid an interconnect bottleneck, quantum integrated circuits hosting the qubits and their electronic control on the same chip have been proposed[2,3,21]. Whereas these architectures provide an elegant way to greatly increase the qubit count by leveraging the success of classical integrated circuits, a key question is whether the qubits will be robust against the thermal noise imposed by the power dissipation of the electronics. Demonstrating a universal gate set at increased temperatures would therefore be a milestone in the effort towards scalable quantum systems. Recently, Yang et al.[8] demonstrated single-qubit control above 1 K with silicon quantum dots, but the crucial two-qubit gate could only be performed at a reduced temperature of 40 mK.

Here, we demonstrate all operations required to execute hot universal quantum logic by combining initialization, readout, single-qubit rotations and two-qubit gates, and we perform full two-qubit logic in a quantum circuit operating at 1.1 K. We furthermore examine the temperature dependence of the quantum coherence, which—unlike the spin relaxation process[6]—we find to be hardly affected in the temperature range T = 0.45–1.25 K.

Figure 1a conceptually displays a quantum integrated circuit. Inspired by its classical counterpart, in which only a few control lines are needed to interact with billions of transistors, a quantum integrated circuit hosts the quantum hardware and its electronic control on the same chip to provide a scalable solution[20]. Here we focus on the quantum hardware of such a circuit, which we implement using silicon quantum dots.

Figure 1b shows the silicon quantum dot device. The qubits are realized in an isotopically purified ^{28}Si epilayer with a ^{29}Si residual concentration of 800 ppm. The fabrication of the quantum dot device is based on an overlapping-gate scheme to allow the integration of tightly confined quantum dots[22,23]. Electrons can be loaded either from the reservoir or from the single-electron transistor (SET)[24], which is also used for charge sensing. To enable coherent control over the electron spins, a.c. currents are applied through the on-chip aluminium microwave antenna.

Figure 1c shows a charge stability diagram of the double quantum dot, where the qubits Q_1 and Q_2 and their coupling are defined by using the gates P_1, B_{12} and P_2. Because we can freely choose the occupancy of the

[1]QuTech and Kavli Institute of Nanoscience, Delft University of Technology, Delft, The Netherlands. [2]Components Research, Intel Corporation, Hillsboro, OR, USA. ✉e-mail: M.Veldhorst@tudelft.nl

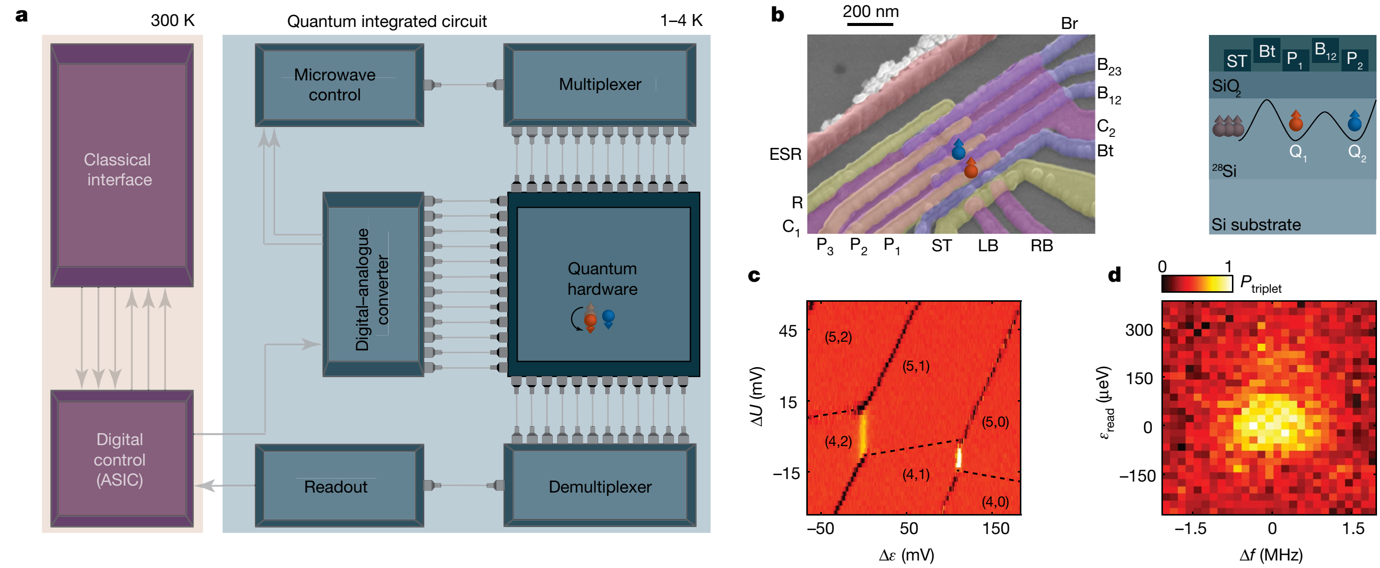

Fig. 1 | Large-scale approach for silicon qubits. a, Quantum integrated circuit hosting the qubits and their control electronics on the same chip. The control functionality that can be integrated is strongly dependent on the available cooling power. When the qubits can be coherently controlled above 1 K, a broad range of electronics may be integrated. At the lowest-temperature stage, multiplexing strategies can be combined with digital-to-analogue converters, microwave control and local readout, so that only digital signals need to be processed at room temperature. Additionally, long-distance spin–qubit coupling mechanisms would allow to build modular architectures in which widely sparsed qubit arrays and local electronics alternate on the same chip, further alleviating fan-out and wiring issues[2]. **b**, Scanning electron microscope image of a quantum device identical to the one measured. Gates P_1 and P_2 define the two quantum dots and gate B_{12} controls the inter-dot tunnel coupling. The SET, defined by the top gate (ST) and the two barriers (RB and LB), is used both as a charge sensor and as a reservoir[24], whereas the tunnel rate is controlled by Bt. Gates C_1 and C_2 confine the electrons in the three quantum dots. Gates R, Br, P_3 and B_{23} are kept grounded during the experiment. The qubits are driven via electron spin resonance (ESR). **c**, Electron occupancy as a function of the detuning energy between the two quantum dots, ε, and on-site repulsion energy, U. The data are centred at the (4, 2)–(5, 1) anticrossing. The electron transitions are measured via a lock-in technique[35], by applying an excitation of 133 Hz on gate B_{12}. Both electrons are loaded from the SET, with Q_2 having a tunnelling rate considerably lower than Q_1. **d**, Probability to detect a triplet state, P_{triplet}, as a function of readout position, $\varepsilon_{\mathrm{read}}$, and microwave frequency applied to Q_2, Δf. When the readout level is positioned between the singlet–triplet energy splitting and the microwave frequency matches the resonance frequency of Q_2, we correctly read out the transition from state $|{\downarrow\uparrow}\rangle$ to the blocked state $|{\uparrow\uparrow}\rangle$.

two quantum dots, we tune to the regime in which we obtain optimal exchange coupling, which we find to have one and five electrons for Q_1 and Q_2, respectively. We then operate the system close to the (5, 1)–(4, 2) charge anticrossing.

Single spins are often initialized via energy-selective tunnelling to a nearby reservoir[25]. However, this method requires a Zeeman splitting much higher than the thermal broadening, limiting the fidelity and making the method impractical for high-temperature operation. Instead, Pauli spin blockade offers a convenient mechanism to perform initialization and readout[2,7], with a relevant energy scale corresponding to the singlet–triplet energy splitting, which is set by the large and tunable valley splitting energy in silicon metal–oxide–semiconductor (SiMOS) devices[26]. This method is more robust against thermal noise and enables independent optimization of the qubit operation frequency. We choose to set the magnetic field to $B = 0.25$ T, which corresponds to addressable qubits with Larmor frequencies $\nu_{Q1} = 6.949$ GHz and $\nu_{Q2} = 6.958$ GHz in the absence of exchange interaction. This low-frequency operation reduces the qubit sensitivity to electrical noise that couples in via spin–orbit coupling[27]. Additionally, it simplifies the demands on the electronic control circuits and reduces the cable losses.

The pulse sequence used in the experiment is schematically shown in Fig. 2a. The sequence starts by pulsing deep into the (4, 2) charge state, where the spins quickly relax to the singlet state. An adiabatic pulse to the (5, 1) regime is applied to initialize the system in the $|{\downarrow\uparrow}\rangle$ state. At this detuning energy ε, single- and two-qubit gate operations are performed by applying a microwave burst with variable frequency and duration. The sequence ends by adiabatically pulsing to the anticrossing where readout is performed. The antiparallel spin state with the lowest energy (which, in this experiment, is the state $|{\downarrow\uparrow}\rangle$) couples directly to the singlet (4, 2) charge state. The remaining antiparallel spin state ($|{\uparrow\downarrow}\rangle$) and the two parallel spin states ($|{\uparrow\uparrow}\rangle$, $|{\downarrow\downarrow}\rangle$) couple to the three triplet (4, 2) charge states. This allows us to map $|{\downarrow\uparrow}\rangle$ and the other basis states to different charge configurations ((4, 2) or (5, 1) states), which can be read out using the SET. As shown in Fig. 1d, the optimal readout position can be obtained by sweeping ε and applying a π-pulse to Q_2. From the detuning lever arm of $\alpha_\varepsilon = 0.044$ eV V^{-1}, extracted from the thermal broadening of the polarization line, we find a readout window of 155 μeV, where we can efficiently discriminate between the singlet and triplet states.

In this high-temperature operation mode, the readout visibility is mainly limited by the broadening of the SET peaks. To maximize the sensitivity, we subtract a reference signal from each trace and then we average and normalize the resulting signal (for more details on the readout see Extended Data Figs. 1, 2).

Figure 2b–g shows the single-qubit characterization of the two-qubit system. We observe clear Rabi oscillations for both qubits (Fig. 2b, c) as a function of the microwave burst duration. From the decay of the Ramsey fringes (Fig. 2d, e) we extract dephasing times $T^*_{2(Q1)} = 2.1$ μs and $T^*_{2(Q2)} = 2.7$ μs, comparable to experiments at similar high temperatures[8]. These times are considerably shorter than the longest reported times[11] for ^{28}Si; however, they are still longer than the dephasing times for natural silicon at base temperature[16,17]. Furthermore, we measure spin lifetimes (see Extended Data Fig. 4) of $T_{1(Q1)} = 2.0$ ms and $T_{1(Q2)} = 3.7$ ms, consistent with values reported in a similar device at a similar operating temperature[6].

We characterize the performance of the single-qubit gates of the two qubits by performing randomized benchmarking[28]. In the manipulation phase, we apply sequences of random gates extracted from the Clifford group, followed by a recovery gate that brings the system to the $|{\downarrow\downarrow}\rangle$ and $|{\uparrow\uparrow}\rangle$ states for Q_1 and Q_2, respectively. By fitting the decay of the readout signal as a function of the number of applied gates to

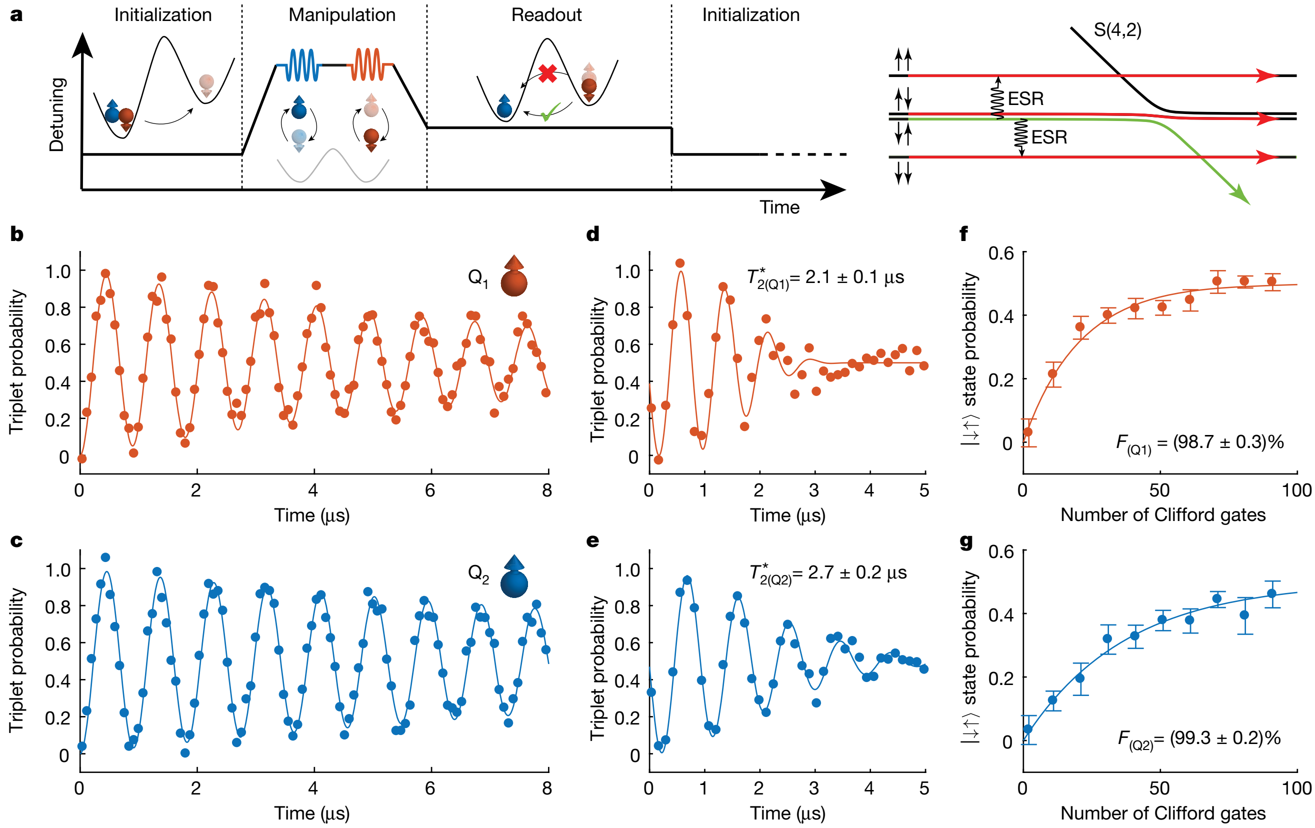

Fig. 2 | Single-qubit characterization at 1.1 K. a, Pulse sequence used for the experiments. Qubits Q_1 and Q_2 are defined on the spin states of single electrons, and the remaining four electrons in Q_2 fill the first levels and do not contribute to the experiment. A voltage ramp allows adiabatic transitions between the (5, 1) and (4, 2) charge states. The antiparallel spin state |↓↑⟩ couples directly with the singlet S(4, 2) state. Each measurement cycle consists of two of these sequences. The second cycle contains no microwave pulses and it is used as a reference to cancel low-frequency drifts during readout. **b**, **c**, Rabi oscillations for both qubits as a function of microwave pulse duration. We extract decay time constants of $T^{\mathrm{Rabi}}_{2(\mathrm{Q1})} = 8$ μs and $T^{\mathrm{Rabi}}_{2(\mathrm{Q2})} = 14$ μs. **d**, **e**, Decay of the Ramsey fringes for both qubits. The data correspond to the average of four traces, and each point is obtained from 500 single-shot traces. **f**, **g**, Randomized benchmarking of the single-qubit gates for both qubits. Each data point is obtained from 500 averages of 20 Clifford sequences, for a total of 10,000 single-shot traces. The fidelity reported refers to the primitive gates, and a Clifford gate contains on average 1.875 primitive gates. We have normalized the state probabilities to remove the readout errors. Error bars are 1 s.d. from the mean.

an exponential decay, we extract qubit fidelities of $F_{\mathrm{Q1}} = (98.7 \pm 0.3)\%$ and $F_{\mathrm{Q2}} = (99.3 \pm 0.2)\%$, with the second one above the fault-tolerance threshold.

We now turn to the two-qubit gate characterization. The ability to tune the exchange interaction[9] is the basis of performing two-qubit operations with electrons in quantum dots. By turning on the exchange interaction, by controlling either the detuning energy or the tunnel coupling, the resonance frequencies of each qubit shift, depending on the spin state of the other qubit. The central inset in Fig. 3a shows this frequency shift for both qubits as a function of the detuning energy between the two quantum dots, with and without a π-pulse applied to flip the spin state of the other qubit. The full exchange spectrum is composed of the transitions f_1 (|↓↑⟩ → |↓↓⟩), f_2 (|↑↑⟩ → |↑↓⟩), f_3 (|↓↓⟩ → |↑↓⟩) and f_4 (|↓↑⟩ → |↑↑⟩). The exchange interaction J can be extracted as the differences $f_2 - f_1$ and $f_4 - f_3$, from which we measure the tunable J to be in the range 0.5–18 MHz (see Fig. 4a). At even larger exchange couplings, the readout visibility drastically reduces, which we attribute to a decrease of T_2^* (see Fig. 4b). By fitting the exchange spectrum (see Supplementary Information section I), we extract a tunnel coupling of $t_c = 0.8$ GHz and a Zeeman energy difference of $\delta E_Z = 9.1$ MHz.

Having demonstrated the tunability of the exchange interaction, we use it to demonstrate two-qubit operation. When the exchange is turned on, the resulting shift in resonance frequency can be used to implement state-selective electron spin resonance transitions (coherent two-qubit controlled rotations, CROT), which are equivalent to a CNOT gate up to single-qubit phases. Figure 3a shows controlled oscillations for both qubits, with the control qubit set to either the spin-down or the spin-up state, where we have set the exchange interaction to $J = 2.5$ MHz. When we prepare the state of the control qubit such that the target qubit is in resonance with the external microwave control, we observe clear oscillations of the target qubit as a function of the microwave burst duration, with no substantial decay after multiple rotations. When we flip the state of the control qubit, the resonance frequency of the target qubit is shifted, and the target qubit is not driven by the microwave control.

To investigate the coherence of the two-qubit logic, we apply a sequence in which we interleave a CROT operation with duration 2π between two π/2 single-qubit gates applied to the control qubit with variable phase θ. As shown in Fig. 3b, when we invert the second π/2 pulse ($\theta = \pi$), this cancels out the π phase left by the CROT operation on the control qubit and we correctly measure transitions to the |↓↓⟩ and |↑↑⟩ states. This demonstrates the execution of a coherent CROT, because the control qubit maintains its coherence even when the target qubit is driven.

To show the universality of our gate set, we also demonstrate two-qubit randomized benchmarking. We apply random gates from the two-qubit Clifford group that contains 11,520 elements. Next, we recover the state to |↓↑⟩ and measure how the singlet probability decays over the number of applied gates. The decay is shown in Fig. 3d and the primitive gates used are presented in Fig. 3c. The lower fidelity, $F = (86.1 \pm 0.6)\%$, compared to the single-qubit benchmark can be attributed to the longer time spent by the qubits idling, which causes them to decohere faster. Possible improvements include simultaneous driving

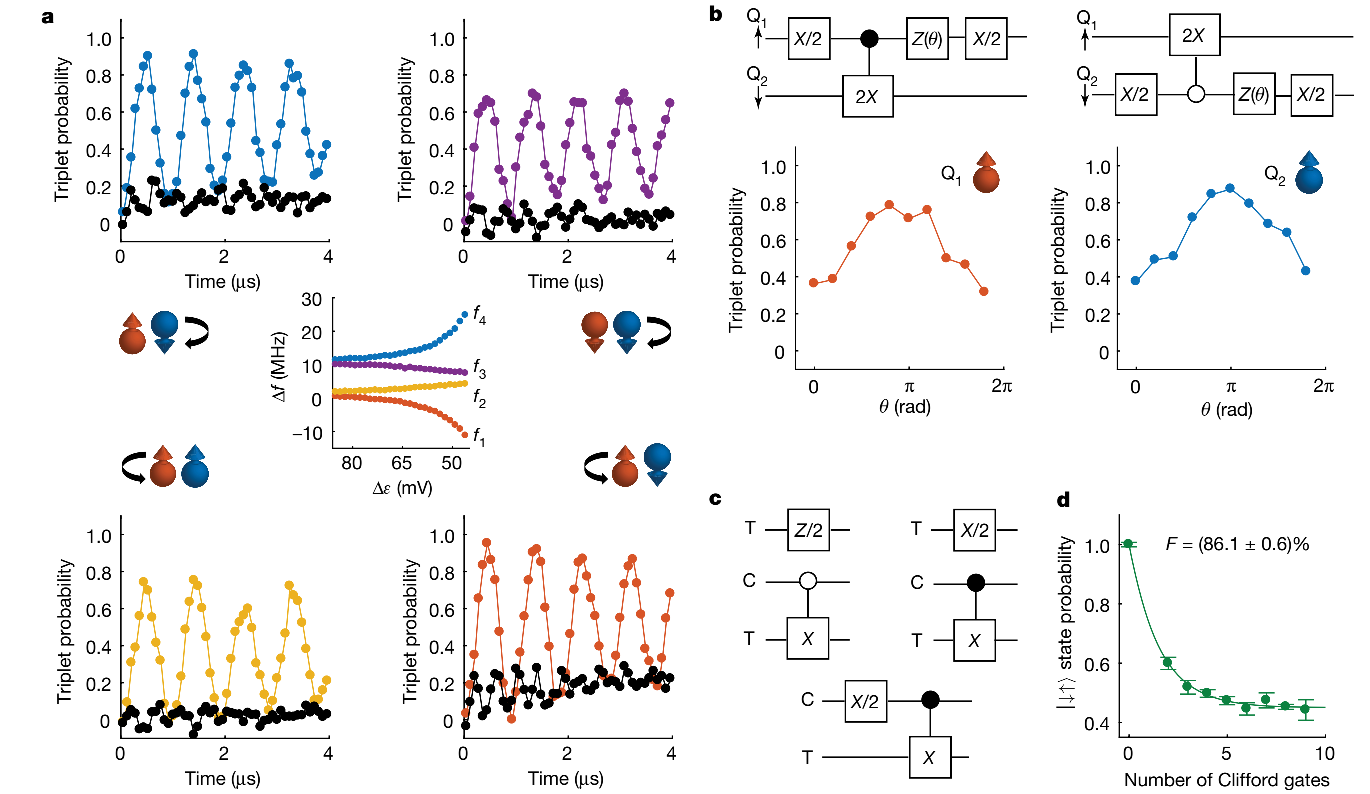

Fig. 3 | Exchange and two-qubit logic at 1.1 K. a, Conditional rotations on all frequencies f_i. The colour code refers to the central inset, which shows the full exchange diagram obtained from a Gaussian fit of the data shown in Extended Data Fig. 3. The frequency offset is 6.948 GHz. The black lines correspond to the same transition f_i, driven with the control qubit in the opposite state. An initialization π-pulse and a recovery π-pulse are applied to the control qubit for the sequences in which either Q_1 is in the spin-down state or Q_2 is in the spin-up state. All Rabi frequencies are set to approximately 1 MHz by adjusting the power of the microwave source to compensate for the frequency-dependent attenuation of the a.c. line carrying the microwave signal. Even when the exchange interaction is turned on, we find the resonance frequencies of both qubits to be stable over the course of several hours (see Extended Data Fig. 5). **b**, Phase acquired by the control qubit during a CROT operation. A CROT gate, together with a Z rotation of π/2 on the control qubit is equivalent to a CNOT operation. Z gates are implemented by a software change of the reference frame. **c**, Primitive gates used to generate the two-qubit Clifford group (11,520 gates in total). On average, each Clifford gate contains 2.5694 primitive gates. Because the $Z/2$ gates are implemented via a software change of the reference frame, they are not included in the gate count. All gates shown in the figure (except for the $Z/2$ gate) are implemented with two π/2 controlled rotations. The compilation scheme is identical to the one in ref. [18]. **d**, Decay of the |↓↑⟩ state probability as a function of the number of two-qubit Clifford gates applied. A recovery gate returns the system to the |↓↑⟩ state. Because we include the recovery gate in the Clifford gate count, the first data point corresponds to two gates applied. Each data point corresponds to the average of 150 random sequences. The fidelity $F = (86.1 \pm 0.6)\%$ corresponds to the average fidelity of the primitve gates shown in **c**. We have normalized the state probabilities to remove the readout errors. Error bars are 1 s.d. from the mean.

of two transitions to reduce idling times, optimized pulse shaping to reduce accidental excitations of nearby transitions, and operation at the symmetry point[29,30].

To further investigate the quantum coherence of the system, we measure the decay of the Ramsey fringes for different values of the exchange interaction; see Fig. 4b. We find that by increasing the exchange interaction the coherence is reduced, which we explain by the increased qubit sensitivity to electrical noise. We can fit the data with a model (see Supplementary Information section II and Supplementary Fig. 1a) that includes quasi-static electrical noise coupling via the exchange interaction and via the Zeeman energy difference between the two qubits. From the fit we extract the fluctuation amplitudes $\delta_\varepsilon = 21\,\mu\text{eV}$ (corresponding to a power spectrum of $A_\varepsilon \approx 6\,\mu\text{eV Hz}^{-1/2}$ at 1 Hz) and $\delta E_Z = 400$ kHz. The noise in ε is comparable to values extracted at fridge base temperature[31] and consistent with charge noise values extracted from current fluctuation measurements of SETs (see Supplementary Information section II for further information)[6,32].

To analyse the thermal impact, we characterize the temperature dependence of T_2^* for two exchange interaction values ($J = 0.5$ MHz and $J = 2.5$ MHz) and we find it to be approximately stable in the range $T = 0.45$–1.25 K (see Fig. 4c). Although weak temperature dependencies of T_2^* have been reported in other single-qubit experiments[8], we observe here that the weak temperature dependence is maintained even when the exchange interaction is set to an appreciable value, where we can perform two-qubit logic.

The electrical noise that limits T_2^* can potentially originate from extrinsic or intrinsic sources. Although we cannot rule out all extrinsic noise sources, we have confirmed that attenuating the transmission lines does not affect T_2^*, and we thus rule out a direct impact of the waveform generator and the microwave source. When intrinsic charge noise is the dominant contribution, a simple model based on an infinite number of two-level fluctuators (TLFs) predicts a square-root dependence of the dephasing rate on the temperature[33]. However, this model assumes a constant activation energy distribution of the TLFs. Deviations from this assumption have been observed in SET measurements, leading to anomalous temperature dependencies[34]. The small size of quantum dots, in particular SiMOS qubits, may lead to only a few TLFs being relevant for the dephasing, and these may explain the observed weak temperature dependence (see Supplementary Information section III for more details).

Importantly, the weak dependence of T_2^* on the temperature makes silicon qubits remarkably robust against thermal noise, enabling the execution of a universal quantum gate set. The ability to operate lithographically defined qubits above 1 K resolves one of the key challenges

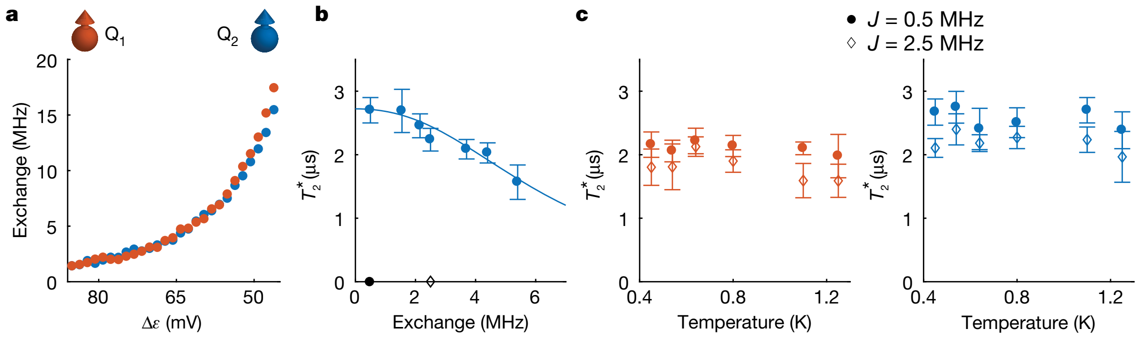

Fig. 4 | Dependence of dephasing on temperature and exchange interaction. a, Exchange energy measured as a function of detuning. The data correspond to $f_2 - f_1$ and $f_4 - f_3$ as obtained from Fig. 3a. **b**, Dephasing time of Q_2 as a function of the exchange interaction, fitted with a model that takes into account Gaussian quasi-static noise (see Supplementary Information section II). Similar data from Q_1 are shown in Extended Data Fig. 6. **c**, Temperature dependence of the dephasing time, with the exhange interaction set to the minimum, obtained by sweeping ε ($J = 0.5$ MHz) and with the exchange interaction set to acquire the CROT operations of Fig. 3a ($J = 2.5$ MHz). Error bars are 1 s.d. from the mean.

towards the integration of quantum hardware and control electronics on the same chip. This integration can reduce the number of lines going from room temperature to the device and, at the same time, greatly simplify on-chip wiring, facilitating the realization of quantum integrated circuits for large-scale quantum computation.

Online content

Any methods, additional references, Nature Research reporting summaries, source data, extended data, supplementary information, acknowledgements, peer review information; details of author contributions and competing interests; and statements of data and code availability are available at https://doi.org/10.1038/s41586-020-2170-7.

1. Ladd, T. D., Jelezko, F., Laflamme, R., Nakamura, Y., Monroe, C. & O'Brien, J. L. Quantum computers. *Nature* **464**, 45–53 (2010).
2. Vandersypen, L. M. K. et al. Interfacing spin qubits in quantum dots and donors—hot, dense, and coherent. *npj Quant. Inf*. **3**, 34 (2017).
3. Veldhorst, M., Eenink, H. G. J., Yang, C. H. & Dzurak, A. S. Silicon CMOS architecture for a spin-based quantum computer. *Nat. Commun*. **8**, 1766 (2017).
4. Devoret, M. H. & Schoelkopf, R. J. Superconducting circuits for quantum information: an outlook. *Science* **339**, 1169–1174 (2013).
5. Neill, C. et al. A blueprint for demonstrating quantum supremacy with superconducting qubits. *Science* **360**, 195–199 (2018).
6. Petit, L. et al. Spin lifetime and charge noise in hot silicon quantum dot qubits. *Phys. Rev. Lett*. **121**, 076801 (2018).
7. Urdampilleta, M. et al. Gate-based high fidelity spin read-out in a CMOS device. *Nat. Nanotechnol*. **14**, 737–741 (2019).
8. Yang, C. H. et al. Operation of a silicon quantum processor unit cell above one kelvin. *Nature* https://doi.org/10.1038/s41586-020-2171-6 (2019).
9. Loss, D. & DiVincenzo, D. P. Quantum computation with quantum dots. *Phys. Rev. A* **57**, 120–126 (1998).
10. Zwanenburg, F. A. et al. Silicon quantum electronics. *Rev. Mod. Phys*. **85**, 961–1019 (2013).
11. Veldhorst, M. et al. An addressable quantum dot qubit with fault-tolerant control-fidelity. *Nat. Nanotechnol*. **9**, 981–985 (2014).
12. Itoh, K. M. & Watanabe, H. Isotope engineering of silicon and diamond for quantum computing and sensing applications. *MRS Commun*. **4**, 143–157 (2014).
13. Yoneda, J. et al. A quantum-dot spin qubit with coherence limited by charge noise and fidelity higher than 99.9%. *Nat. Nanotechnol*. **13**, 102–106 (2018).
14. Yang, C. H. et al. Silicon qubit fidelities approaching incoherent noise limits via pulse engineering. *Nat. Electron*. **2**, 151–158 (2019).
15. Veldhorst, M. et al. A two-qubit logic gate in silicon. *Nature* **526**, 410–414 (2015).
16. Zajac, D. M. et al. Resonantly driven CNOT gate for electron spins. *Science* **359**, 439–442 (2018).
17. Watson, T. F. et al. A programmable two-qubit quantum processor in silicon. *Nature* **555**, 633–637 (2018).
18. Huang, W. et al. Fidelity benchmarks for two-qubit gates in silicon. *Nature* **569**, 532–536 (2019).
19. Fowler, A. G., Mariantoni, M., Martinis, J. M. & Cleland A. N. Surface codes: towards practical large-scale quantum computation. *Phys. Rev. A* **86**, 032324 (2012).
20. Franke, D. P., Clarke, J. S., Vandersypen, L. M. K. & Veldhorst, M. Rent's rule and extensibility in quantum computing. *Microprocess. Microsyst*. **67**, 1–7 (2019).
21. Li, R. et al. A crossbar network for silicon quantum dot qubits. *Sci. Adv*. **4**, eaar3960 (2018).
22. Lawrie, W. I. L. et al. Quantum dot arrays in silicon and germanium. *Appl. Phys. Lett*. **116**, 080501 (2020).
23. Angus, S. J., Ferguson, A. J., Dzurak, A. S. & Clark, R. G. Gate-defined quantum dots in intrinsic silicon. *Nano Lett*. **7**, 2051–2055 (2007).
24. Morello, A. et al. Single-shot readout of an electron spin in silicon. *Nature* **467**, 687–691 (2010).
25. Elzerman, J. M., Hanson, R., Van Beveren, L. W., Witkamp, B., Vandersypen, L. M. K. & Kouwenhoven, L. P. Single-shot read-out of an individual electron spin in a quantum dot. *Nature* **430**, 431–435 (2004).
26. Yang, C. H. et al. Spin-valley lifetimes in a silicon quantum dot with tunable valley splitting. *Nat. Commun*. **4**, 2069 (2013).
27. Ruskov, R., Veldhorst, M., Dzurak A. S. & Tahan, C. Electron g-factor of valley states in realistic silicon quantum dots. *Phys. Rev. B* **98**, 245424 (2018).
28. Magesan, E., Gambetta, J. M. & Emerson, J. Scalable and robust randomized benchmarking of quantum processes. *Phys. Rev. Lett*. **106**, 180504 (2011).
29. Reed, M. D. et al. Reduced sensitivity to charge noise in semiconductor spin qubits via symmetric operation. *Phys. Rev. Lett*. **116**, 110402 (2016).
30. Martins, F. et al. Noise suppression using symmetric exchange gates in spin qubits. *Phys. Rev. Lett*. **116**, 116801 (2016).
31. Güngördü, U. & Kestner, J. P. Pulse sequence designed for robust *C*-phase gates in SiMOS and Si/SiGe double quantum dots. *Phys. Rev. B* **98**, 165301 (2018).
32. Freeman, B. M., Schoenfield, J. S. and Jiang, H. Comparison of low frequency charge noise in identically patterned Si/SiO_2 and Si/SiGe quantum dots. *Appl. Phys. Lett*. **108**, 253108 (2016).
33. Paladino, E., Galperin, Y. M., Falci, G. & Altshuler, B. L. 1/*f* noise: implications for solid-state quantum information. *Rev. Mod. Phys*. **86**, 361–418 (2014).
34. Connors, E. J., Nelson, J. J., Qiao, H., Edge, L. F. & Nichol, J. M. Low-frequency charge noise in Si/SiGe quantum dots. *Phys. Rev. B* **100**, 165305 (2019).
35. Yang, C. H., Lim, W. H., Zwanenburg, F. A. & Dzurak, A. S. Dynamically controlled charge sensing of a few-electron silicon quantum dot. *AIP Adv*. **1**, 042111 (2011).

Methods

Experimental setup

All measurements are performed in a Bluefors dry dilution refrigerator with a base temperature of $T_{\mathrm{base}} \approx 0.45$ K, operated at $T = 1.1$ K. The d.c. voltages are applied using battery-powered voltage sources and the a.c. voltages are applied through a bias-tee on the sample printed circuit board with a cut-off frequency of 3 Hz. The pulse sequences are generated by an arbitrary waveform generator (AWG; Tektronix AWG5014C) combined with a microwave signal generated by a Keysight PSG8267D vector source. Electron spin resonance (ESR) currents are delivered via the vector source using the internal IQ mixer, driven by two output channels of the AWG. Both qubits can be addressed by setting the vector source to an intermediate frequency and IQ-mixing the signal with a (co-)sine wave generated on channels 3 and 4 of the AWG. For the two-qubit randomized benchmarking experiment, the pulse sequences are generated by a Keysight M3202A AWG, which allows faster waveform uploads. We apply a source–drain bias voltage of $V_{\mathrm{SD}} = 0.5$ mV to the single-electron transistor and measure the current using an in-house-built transimpedance amplifier.

Single-qubit randomized benchmarking

The single-qubit Clifford group C_1 consists of 24 rotations. We implement the group using X and Y rotations, using the primitive gates: $\{I, \pm X/2, \pm Y/2, \pm X, \pm Y\}$. On average one Clifford gate contains 1.875 primitive gates. We implement the gates using only frequencies f_1 and f_4 for Q_1 and Q_2, respectively. The complete list of gates is given in Extended Data Table 1.

The phase control needed to implement X and Y rotations is achieved using the internal IQ mixer of the microwave source. The fidelity reported in the main text refers to the average fidelity of the gates in the generator group.

Two-qubit randomized benchmarking

The two-qubit Clifford group C_2 consist of 11,520 elements c_2 with properties $c_2^{\dagger} P c_2 \in \pm P$, where P are the Pauli operators. We generate the Clifford gates in our experiment using the set of conditional rotations in Fig. 3a, where two subsequent conditional rotations implement a primitive gate. We compile the Clifford gates from the set of primitive gates together with virtual $Z/2$ gates on both qubits and search for combinations with the minimal number of gates. The resulting average Clifford gate consists of 2.5694 primitive gates, which are calibrated so that each conditional rotation takes exactly 330 ns, with the exchange interaction set to 3 MHz. To minimize cross-talk, the timing and the exchange interaction are chosen such that the off-resonant pulse is synchronized with the resonant pulse.

Data availability

All data underlying this study will become available on the 4TU ResearchData repository, https://doi.org/10.4121/uuid:22653416-85b0-4d7d-ad48-65967f9ea7ad.

36. Eenink, H. G. J. et al. Tunable coupling and isolation of single electrons in silicon metal-oxide-semiconductor quantum dots. *Nano Lett*. **19**, 8653–8657 (2019).

Acknowledgements We thank J. Helsen for developing the code for the compilation of the two-qubit Clifford group. We additionally thank M. Mehmandoost and V. V. Dobrovitski for discussions and suggestions. L.P., H.G.J.E. and M.V. are funded by a Netherlands Organization of Scientific Research (NWO) VIDI grant. Research was sponsored by the US Army Research Office (ARO) and was accomplished under grant number W911NF-17-1-0274. The views and conclusions contained in this document are those of the authors and should not be interpreted as representing the official policies, either expressed or implied, of the Army Research Office (ARO), or the US Government. The US Government is authorized to reproduce and distribute reprints for Government purposes notwithstanding any copyright notation herein.

Author contributions L.P. and H.G.J.E. performed the experiment. H.G.J.E. fabricated the device. W.I.L.L. contributed to the process development; N.W.H. and S.G.J.P. contributed to the preparation of the experiment. J.S.C. supervised the wafer growth. L.P. and M.R. analysed the results with input from all authors. L.M.K.V. and M.V. conceived the project. L.P. and M.V. wrote the manuscript with input from all authors. M.V. supervised the project.

Competing interests The authors declare no competing interests.

Additional information
Supplementary information is available for this paper at https://doi.org/10.1038/s41586-020-2170-7.
Correspondence and requests for materials should be addressed to M.V.
Peer review information *Nature* thanks HongWen Jiang and the other, anonymous, reviewer(s) for their contribution to the peer review of this work.
Reprints and permissions information is available at http://www.nature.com/reprints.

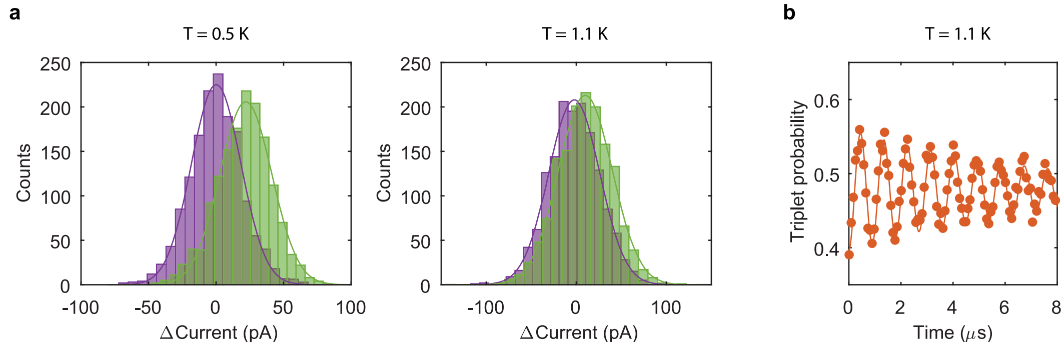

Extended Data Fig. 1 | Charge readout and visibility. a, Histograms of the readout signal for the singlet and triplet state for two operating temperatures. The sensitivity is reduced at higher temperatures, mainly because of the thermal broadening of the Coulomb peaks. The readout signal is obtained by subtracting a reference line obtained from a sequence with no microwave pulse applied. The integration time corresponds to 40 μs. The readout fidelity may be improved by optimizing the charge sensing[36] and by using a radiofrequency reflectometry or dispersive measurement scheme, as shown in ref. [7]. **b**, Rabi oscillations of Q_1 (see also Fig. 2b), obtained by assigning the state spin-up or spin-down to each single-shot trace, by using a threshold obtained from the histograms in **a**. From the data we can extract the visibility, which we find to be $V \approx 0.2$ at $T = 1.1$ K.

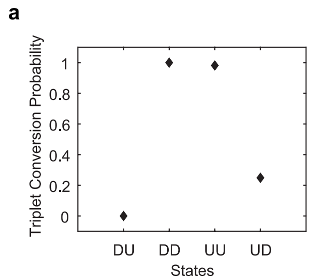

Extended Data Fig. 2 | Spin-to-charge conversion. a, Normalized probability of detecting the four two-electron spin states as a triplet state (U, spin up; D, spin down). The probability that the triplet antiparallel spin state is correctly identified as a triplet can be reduced by the non-perfect adiabaticity of the pulse and by a faster triplet–singlet relaxation.

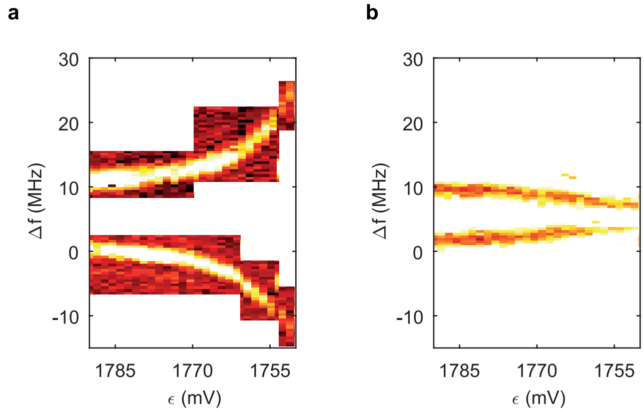

Extended Data Fig. 3 | Exchange interaction. a, **b**, Resonance frequency of both qubits as a function of the detuning energy. **a**, Transitions f_1 and f_4. **b**, Transitions f_2 and f_3. We measure the excited states by ESR-controlled spin flips applied to the control qubit.

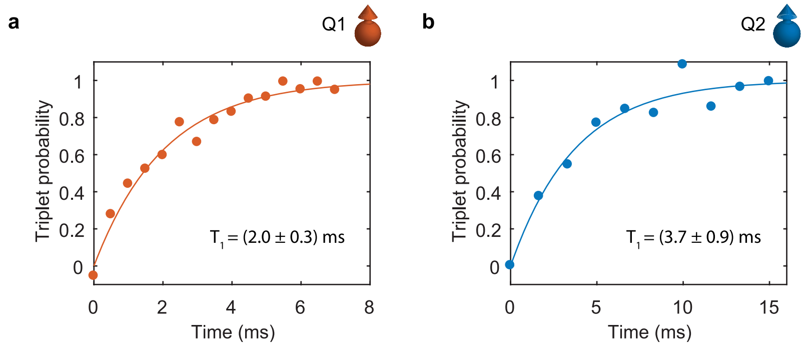

Extended Data Fig. 4 | Relaxation times. a, **b**, Single-spin relaxation times of Q_1 and Q_2. The measurements are performed by fitting the decay of the states $|{\downarrow\uparrow}\rangle$ and $|{\uparrow\downarrow}\rangle$ to state $|{\downarrow\downarrow}\rangle$. We extract $T_{1(Q1)} = 2.0$ ms and $T_{1(Q2)} = 3.7$ ms, consistent with ref. [6]. Triplet probabilities have been normalized to remove readout errors.

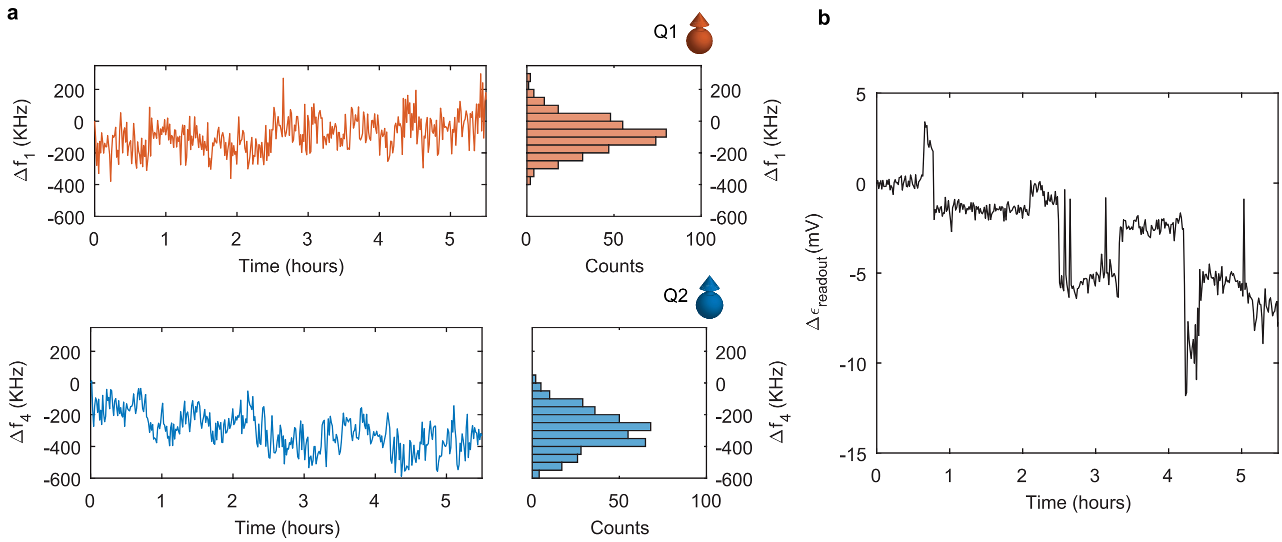

Extended Data Fig. 5 | Time dependence of the resonance frequencies and the readout point. a, Time dependence of the resonance frequencies f_1 and f_4 of Q_1 and Q_2, respectively. The exchange interaction is set to 2.5 MHz. The data have been offset by 6.9491 GHz and 6.9620 GHz for f_1 and f_4, respectively. **b**, Time dependence of the readout point obtained by sweeping along the detuning axis in a measurement identical to the one shown in Fig. 1d. The best readout point is achieved with a Gaussian fit of the visibility peak.

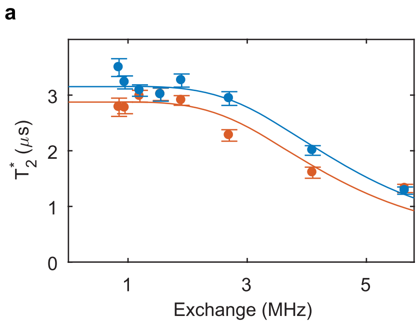

Extended Data Fig. 6 | Dephasing times for Q_1 and Q_2 as a function of exchange interaction. a, Dephasing times of Q_1 and Q_2 as a function of exchange interaction, fitted with the model discussed in Supplementary Information section II. Because of the different tuning configuration, the dephasing times are slightly longer than the ones reported in the main text. In this configuration, we measure a tunnel couping of $t_c = 0.8$ GHz and a Zeeman energy difference of $\delta E_Z = 10.6$ MHz. Error bars are 1 s.d. from the mean.

Extended Data Table 1 | Complete list of gates used in the single-qubit randomized benchmarking

Single-qubit Cliffords						
I	X/2, Y/2	Y/2, X/2	X/2	Y/2	X, Y/2	Y, X/2
X	X/2, -Y/2	Y/2, -X/2	-X/2	-Y/2	X, -Y/2	Y, -X/2
Y	-X/2, Y/2	-Y/2, X/2	-X/2, Y/2, X/2		X/2, Y/2, X/2	
Y, X	-X/2, -Y/2	-Y/2, -X/2	-X/2, -Y/2, X/2		-X/2, Y/2, -X/2	